ADVANCED FUNCTIONAL MATERIALS
www.afm-journal.de

Flexibility and Dynamicity Enhances and Controls Supramolecular Self-Assembly of Zinc(II) Metallogels

*Merlin R. Stühler, Hesam Makki, Dorothee Silbernagl, Mathias Dimde, Kai Ludwig, Bengt E. Tegner, Christopher Greve, Konstantin Rausch, Eva M. Herzig, Anna Köhler, and Alex J. Plajer**

Supramolecular self-assembly of stacked architectures is typically achieved through hydrogen bonding or π–π interactions between monomers constructed from stable and inert bonds. In contrast, coordinative interactions of early metals promise distinct self-assembly behaviour due to more flexible bonding geometries and a wider range of stabilities and exchange kinetics. In this report we demonstrate that tailoring the flexible coordination sphere of Zinc(II) complexes via subtle ligand modification promotes not only one but also three-dimensional self-assembly both thermodynamically and kinetically into higher-order fibrous morphologies, the latter being elucidated by electron tomography. As a result, coordination chemistry can be translated into both nanoscopic (fibre stiffness) and macroscopic (thermal gel stability) material properties. Utilizing dynamicity enables gelation via subcomponent self-assembly, constructing the supramolecular polymer network simultaneously with the monomer. Furthermore, coordinative dis- and reassembly via metal-ligand exchange reactions involving the first and second coordination spheres allows for control over gelation and emission of the system. Our report links concepts in supramolecular self-assembly and coordination chemistry by leveraging the unique bonding interactions that cannot be achieved for traditional monomers, promising applications in stimuli-responsive optoelectronics.

1. Introduction

Supramolecular self-assembly has emerged as an efficient approach for assembling simple molecular building blocks via non-covalent interactions into complex nanostructures.[1–7] Assembly typically occurs through hydrogen bonding or π–π interactions, forming stacked architectures (**Figure 1a**) from monomers that are constructed by robust covalent bonds.[8–22] Metal containing monomers, often involving late transition metals, are also employed for stacking, interacting via metallophilic interactions, yet due to their high ligand field stabilization energy, the involved metal-ligand interactions and geometries again tend to be stable, rigid, and inert.[23–37] In contrast, monomers constructed from lighter metals usually focus on metalated porphyrins in which self-assembly is mainly driven by π–π interactions or requires further support via hydrogen bonding, ionic interactions and amphiphilicity via covalently attached

M. R. Stühler, A. J. Plajer
Makromolekulare Chemie
Universität Bayreuth
Universitätsstraße 30, 95447 Bayreuth, Germany
E-mail: alex.plajer@uni-bayreuth.de

M. R. Stühler, M. Dimde, K. Ludwig
Intitut für Chemie und Biochemie
Freie Universität Berlin
Fabeckstraße 34–36, 14195 Berlin, Germany

H. Makki, B. E. Tegner
Department of Chemistry and Materials Innovation Factory
University of Liverpool
Liverpool L69 7ZD, UK

D. Silbernagl
Bundesanstalt für Materialforschung und -Prüfung (BAM)
Unter den Eichen 87, 12205 Berlin, Germany

C. Greve, E. M. Herzig
Dynamics and Structure Formation
Universität Bayreuth
Universitätsstraße 30, 95547 Bayreuth, Germany

K. Rausch, A. Köhler
Institut für Physik
Universität Bayreuth
Universitätsstraße 30, 95447 Bayreuth, Germany

A. Köhler, A. J. Plajer
Bayrisches Polymer Institut (BPI)
Universität Bayreuth
Universitätsstraße 30, 95447 Bayreuth, Germany

The ORCID identification number(s) for the author(s) of this article can be found under https://doi.org/10.1002/adfm.202507793

DOI: 10.1002/adfm.202507793

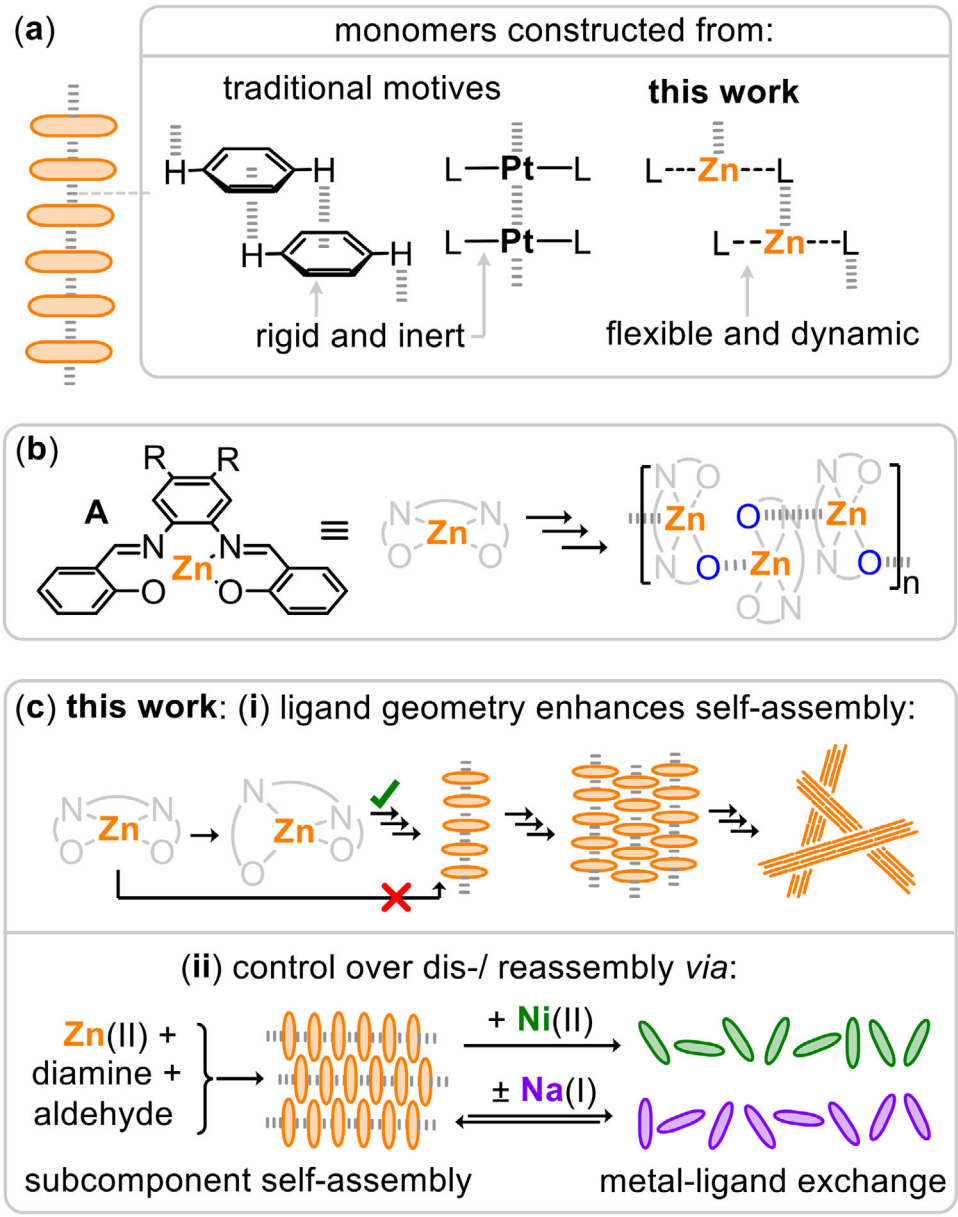

Figure 1. a) Outset of bond types constructing monomers for self-assembly. b) Hypothesis outlined in the literature of Zinc(II) Salphen complexes undergoing stacking. c) Key concepts established in this contribution arising from the bond type characteristics. M = metal, L = ligand, R = alkyl chain.

appendices.[38–46] In these systems some control over the self-assembly by leveraging coordination chemistry of the transition metal is possible via additional coordination sites either attached to the porphyrin scaffold or added as a separate species.[47–49] However, the porphyrin ligand scaffold does not easily allow to alter the coordination environment of the metal in order to control self-assembly since its geometry is rigid, synthetically non-trivial to alter, and because of the likely negligible contributions of metal-ligand coordination between complexes to self-assembly. Nevertheless, 3d-metal-containing monomers promise (i) more flexible coordination environments and thus variable or adaptable monomer geometries provided that the ligand is sufficiently adjustable, as well as (ii) a broader range of interaction strengths and dynamicity (i.e., exchange constants) than the state of the art. Therefore, they provide access to untapped chemical space for supramolecular self-assembly.

In this context, zinc(II) complexes of aryloxy imine ligands have demonstrated self-assembly phenomena such as Zn(II) complex **A** (Figure 1b), that forms organogels in non-coordinating solvents via aggregation into fibrous morphologies.[50–57] Complexes featuring two coordination pockets show self-assembly on pyrolytic graphite surfaces into long lamellar arrays of stacked molecules, while dynamic light scattering in non-coordinating solvents also reveals aggregation in solution.[58] In both cases, computational modelling suggests that a coordinative interaction between the oxygen of one ligand

and the Zn(II) centre of another Salphen ligand is responsible for the self-assembly behaviour, forming $(ZnO)_n$ motifs within supramolecular stacks of the complex that feature pentacoordinate Zn(II) centers. Confirming that coordinative interactions drive self-assembly, the addition of excess pyridine as a competitive donor led to full occupation of all Zn(II) coordination sites, forming pyridine adducts of the complexes that do not self-assemble.

In this study, we introduce a design strategy that uniquely combines the well-established self-assembly behavior of Zn(II) salphen complexes and deliberate modulation of supramolecular interactions through positional isomerism of naphthyl units. The coordination chemistry of Zn(II) is specifically harnessed to direct self-assembly, establishing a conceptual link between ligand design, supramolecular organization, and macroscopic gelation. This level of integration and tunability cannot be readily achieved using conventional hydrogen-bonded or π–π stacked systems in the absence of metal-mediated interactions.

2. Results and Discussion

In order to investigate how the coordination environment affects self-assembly, we prepared a series of complexes **B**, **C**, and **D** in which the previously reported parent complex **A** is formally equipped with π-expanded naphthyl units in different isomeric forms.[53] The complexes were prepared via imine condensation of the alkoxy substituted phenylene diamine with two equivalents of the respective aldehyde and $Zn(OAc)_2(H_2O)_2$ in THF delivering quantitative access to the complexes in high purity which was confirmed by multinuclear NMR and ESI-MS (see ESI Section S2). In reference to previous studies, self-assembly relies on a non-coordinating environment that leaves the Zn(II) centres unoccupied for stacking via Zn-O interactions, and this is generally fulfilled in aromatic solvents including benzene, toluene, and mesitylene to the same extent.[53] As shown in **Figure 2**, self-assembly experiments in toluene (3 mg/mL) show distinct behaviours. Other non-polar aromatic solvents (e.g., benzene) are equally suitable.[53] While **B** forms a stable organogel upon slow cooling a solution from 80 °C to room temperature, **C** and **D** do not. Furthermore, the gel of **B** is more thermally stable than that of **A**, in that liquefaction occurs at ca. 20 °C earlier for the latter upon heating (see below for quantification). Hence, we seeked to establish how the ligand chemistry controls self-assembly in the following.

Firstly, variable temperature ^{1}H NMR spectroscopy in benzene-d_6 gives insights into the mechanism of self-assembly of **A** and **B** (see ESI Figures S25, S26, respectively). Gradual cooling from 75 °C to room temperature in 1 °C steps shows a substantial broadening of the signals of **B** to an extent that certain resonances such as the —CH=N— imine hydrogen cannot be identified. Here, the imine hydrogen resonances in close proximity to the Zn(II) centres exhibit a shift of 0.23 ppm upon cooling while aryl hydrogen resonances shift by less than 0.12 ppm with decreasing tendency the further these are from the Zn(II) centres and the same trend is observed with regards to signal broadness. Heating to 75 °C resolves the full spectrum again. A characteristic temperature at which the signal disappears is found around 65 °C. Accordingly, a similar behavior

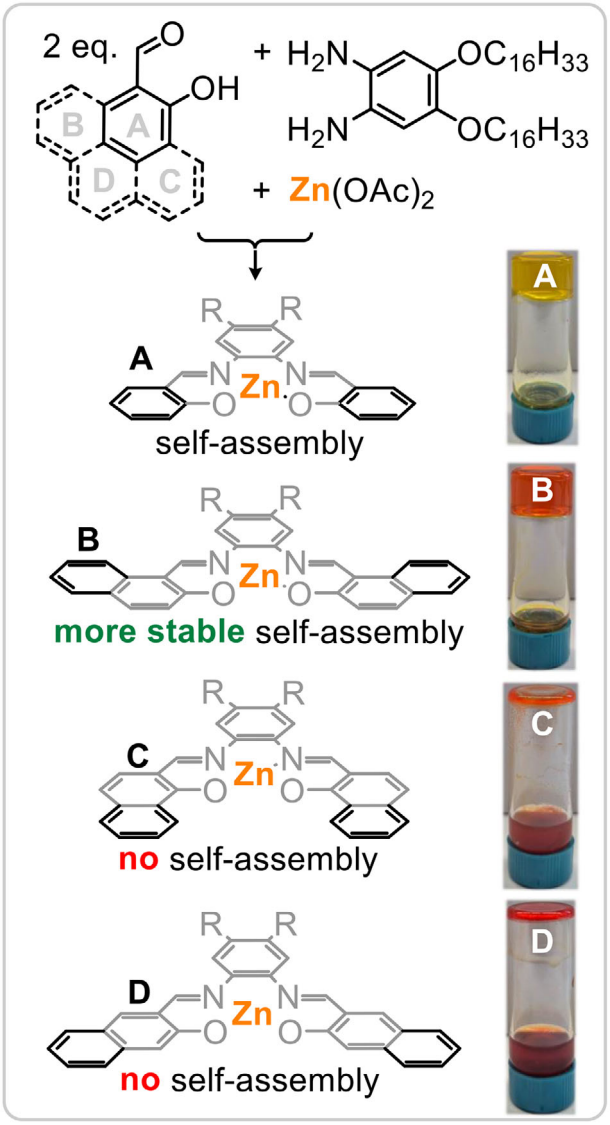

Figure 2. Synthetic scheme and self-assembly behaviour of the complexes A – D.

was observed for **A** with a significantly smaller shift of the imine signal of 0.01 ppm and an onset temperature of around 48 °C.

To further investigate the assembly behaviour of **B**, we turned to absorption and emission spectroscopy (see ESI Figures S27–S30). Interestingly, changes in absorption are negligible with respect to concentration and temperature in toluene. Likewise, the emission spectrum remains unchanged with concentration and temperature. While the spectrally integrated emission intensity decreases with temperature, this decrease is linear. Such a continuous decrease of photoluminescence (PL) intensity is typical for a continuous increase in the non-radiative decay channel, e.g. by thermal activation of vibrations. This, together with the lack of spectral change with concentration, shows that there is no interaction between the π-systems of the ligand in stacks of **B**, and that exclusively metal-ligand coordination controls association of the monomers. This is in line with the

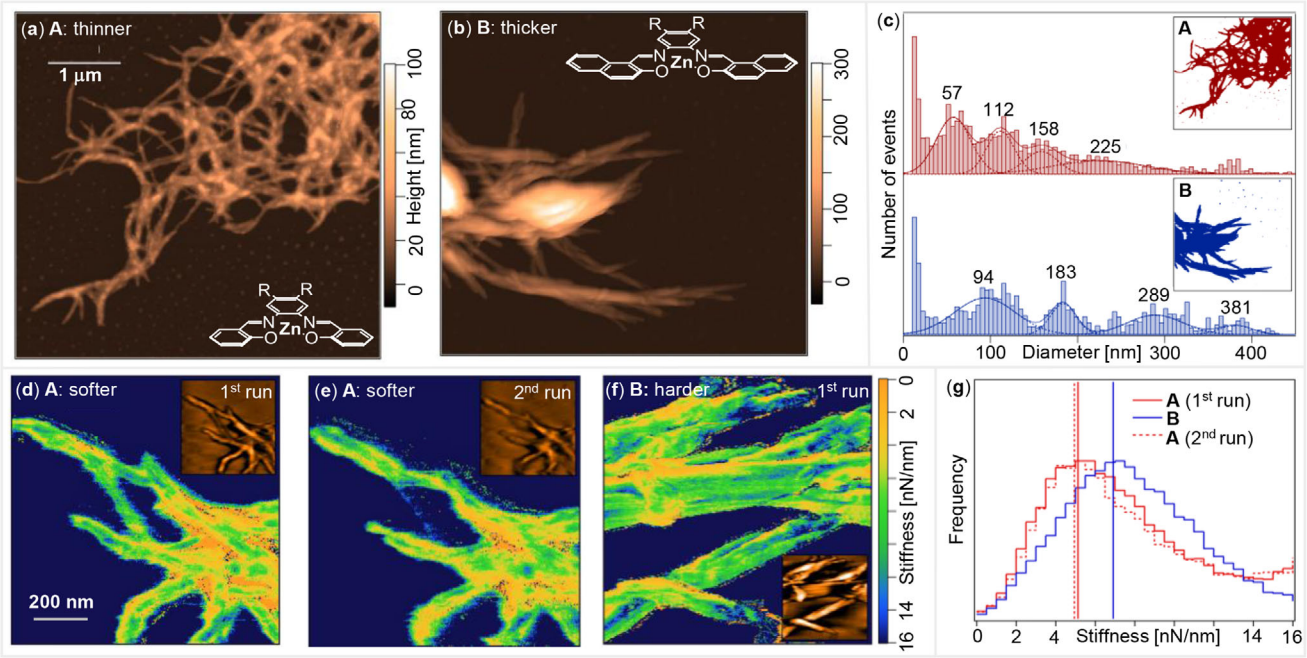

Figure 3. AFM tapping mode topography (1024 × 1024 points, 5 × 5 µm^2) of (a) **A** and (b) **B**. c) Histogram of local diameters (bar plot) acquired from transformed tapping mode images. Gaussian fits of histogram (dashed lines) with annotated fit center (x_0) and fit sum (solid line). Stiffness (k_{eff}) maps (256 × 256 points on a 1 × 1 µm^2 area) of (d) **A** (1st measurement) (e) **A** (2nd measurement) and (f) **B**. (g) Histogram of k_{eff}, mean values are shown by vertical lines.

observation by variable temperature NMR that the temperature-dependent shift of imine hydrogen resonances sitting closest to the Zn(II) centres are most pronounced. Accordingly, **B** does not assemble in pyridine-d_5 producing sharp spectra and the Ni(II) version **B'**, prepared employing $Ni(OAc)_2$ in place of $Zn(OAc)_2$ during synthesis, does not assemble in benzene-d_6 either.

Combined, this implies that although $\pi-\pi$ interactions between complexes do not play a role in the assembly of **A**-**D**, the π−system of the ligand nevertheless is of central importance in enhancing and controlling the self-assembly process and thus the gelation ability. To investigate self-assembly further we turned to atomic force microscopy (AFM). Samples were prepared by spin-coating dilute solutions onto a silicon wafer.

As shown in **Figure** 3a for **A** and Figure 3b for **B** fibrous morphologies are formed, with qualitative differences in diameter observable at a resolution of 5 nm per pixel. For statistical analysis of the fibre thicknesses for **A** and **B**, the topography images were transformed using a height cut-off and evaluated with an algorithm designed as part of the current study (see ESI Section S5 for details). As shown in Figure 3c, this allowed the creation of histograms to quantitatively assess the observed fibre thicknesses. Interestingly, in both **A** and **B**, the histograms reveal peaks at discrete diameter values rather than a statistical distribution of diameters and the histograms could be fitted to a series of Gaussian distributions. The first peak, corresponding to diameters <20 nm, was disregarded as it likely stems from noise and residual monomer. Notably, the analysis revealed smaller structures distributed around a peak thickness, x_0, which aggregate into larger structures with thicknesses approximately $2x_0$, $3x_0$, and $4x_0$.

A forms intrinsically smaller structures with $x_0 = 57$ nm, compared to $x_0 = 94$ nm for **B**. In both cases, x_0 significantly exceeds the expected diameter of a single stack of the complexes which are to exhibit a maximum diameter of approximately 6 nm. This suggests that stacks of **A** and **B** undergo further aggregation, forming higher-order assemblies. Hence AFM clearly shows that stacks of **B** are more prone to aggregation than **A**, as indicated by the greater average thickness of its smallest aggregates.

Moreover, fibres of **B** are stiffer than fibres of **A** as seen in their high-resolution stiffness maps acquired by intermodulation AFM (ImAFM). For this, the local effective stiffness (k_{eff}) was obtained for each pixel of a selected area of the AFM image by amplitude dependent force spectroscopy (Figure 3d–f, for details see ESI Section S5).[59] The histograms of k_{eff} (Figure 3g) reveal that fibres of **A** ($k_{eff,av.}$ = 5.1 nN/nm) are more compliant than fibres of **B** ($k_{eff,av.}$ = 6.9 nN/nm). Furthermore, the scanning motion of the measurement changes the morphology of **A** meaning that parts of the structure were even moved (see Figure 3d compared to (e)). As $k_{eff,av.}$ is maintained it is inferred that the material is not degrading. In contrast, the morphology of **B** remains unchanged during ImAFM. Combined, these findings suggests that **B** exhibits a higher propensity for self-assembly forming thicker and more robust fibres than **A** does.

Transmission electron microscopy (TEM) and electron tomography (ET) helped to shed further light on the differences in assembly behaviour. Previously, TEM measurements of **A** were obtained from MeOH solutions.[53] Although MeOH is a coordinating solvent, slow evaporation during sample preparation suffices to induce self-assembly. As **B** exhibits decreased solubility in MeOH, we employed THF in TEM studies. As can be

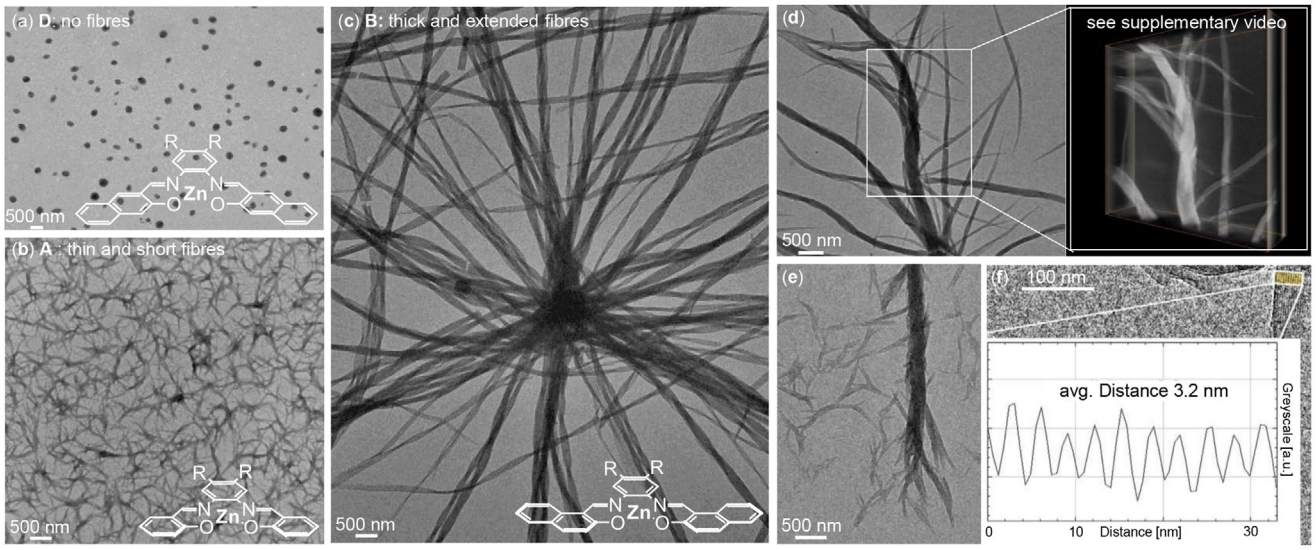

Figure 4. TEM images of (a) **D**, (b) **A,** and (c) **B** all at magnification factor x3400 and deposited from THF solution. d) Electron tomography: "Voltex" presentation of a reconstructed 3D volume calculated from a tilt series (± 64°, 2° increment), recorded from the region of interest marked by a white rectangle in the left micrograph (for details see the supplementary movie file). e) Build-up of bundles from fibres comprising (f) homogeneously stacked layers of complex **B**, distance determined by a profile plot of the gray values.

seen in **Figure** 4 complexes **A** and **B** form distinct fibrous morphologies while the non-stacking complex **D** only forms undefined agglomerates (Figure 4a). **A** forms a network of flexible and irregular fibres with diameters of approximately 10 to 50 nm (Figure 4b) from THF analogous to previous observation of structures formed from MeOH. Remarkably **B** again exhibits a clear tendency for higher-order assembly (Figure 4c) in that smaller fibres assemble into bundles with multiple hundred nm thickness and at least tens of microns in length exceeding the display window of the measurement. Electron-tomography clearly reveals that shorter fibres entwine in a rope-like fashion to build-up the µm length fibres (Figure 4d, see supplementary Video V01). Furthermore, smaller fibres formed by **B** are substantially more rigid and regular than the similar scale fibres of **A** that span the network. As shown in Figure 4e the smaller fibres of **B** comprise a regular parallel arrangement of stripes of increased electron density in an average distance of approximately 3.2 nm. This is furthermore confirmed by Fourier transform analysis revealing formation of a regular lattice with this spacing distance. This distance approximately equates the length of a complex of **B** assuming a stretched conformation of the alkyl substituents. Hence, we infer that the areas of increased electron density correlate to individual stacks of **B** which are parallelly oriented by the interdigitating alkyl substituents of the complex backbone. Combined, TEM thereby reveals that self-assembly of **B** occurs via stacking of complexes that parallelly assemble into shorter rigid fibres which then aggregate into micrometer length bundles. In contrast fibres of **A** are more flexible and less prone to assembly into bundles and this is in line with results by AFM regarding assembly behaviour in solution.

The distinct tendency for self-assembly translates to macroscopic properties of solutions of the complexes at 3 mg/mL in toluene (**Figure** 5a). As previously reported for **A**, **B** forms an organogel upon cooling a solution from 80 °C to RT. In contrast, **C** and **D** partially precipitate without gelation. Temperature-dependent rheology heating curves between 20 and 80 °C show that gels from **B** maintain intact ($G' > G''$) up to ca. 75 °C, while the gel formed from **A** breaks down at ca. 55 °C. Due to the high electron density of the Zinc centres, static wide angle X-ray scattering (WAXS) could be employed to examine the self-assembled structure of the gel in the native state (see ESI Section S7). As shown in Figure 5c, the radially averaged and background corrected WAXS profiles exhibit two distinct scattering peaks between $q = (0.1 - 0.5)$ Å^{-1} for gels of **B** and **A**. The low q peak correlates to regular occurring distances between 3.34−3.47 ± 0.05 nm for **B** and 3.21−3.24 ± 0.02 nm for **A** and this agrees well with the distances observed by TEM which we attributed to the parallel association of stacks. Importantly, this confirms formation of bundles of individual polymer strands into fibres in the native gel state. Upon heating the intensity of these peaks decreases and vanishes at ca. 52 °C for **A** and 74 °C for **B** (Figure 5d). Micro differential calorimetry (μDSC) confirms this (Figure 5e and ESI Figure S38), exhibiting endothermic peaks around these respective temperatures. Combined, we infer that the self-assembled structures of **B** are more thermodynamically stable than those of **A**. We attribute this to stronger interactions between the complexes in the stacks. Viewed in terms of supramolecular polymerisation the sudden onset of assembly suggests a cooperative mechanism for which the onset temperature of **B** is roughly 20 °C higher than for **A**, although the limited spectroscopic changes (vide supra) prevent deeper quantitative evaluation. Therefore, the differences in macroscopic thermal gel stability directly result from variations in aggregation propensity. On a side note, while **A** forms a clear gel, **B** forms a turbid gel which we infer is due to the formation of larger scale aggregates in the case of **B**. Turbidity is rate dependent in that slower cooling results in decreased transmission and a shifted onset of turbidity to higher temperatures. This indicates a kinetically controlled self-assembly

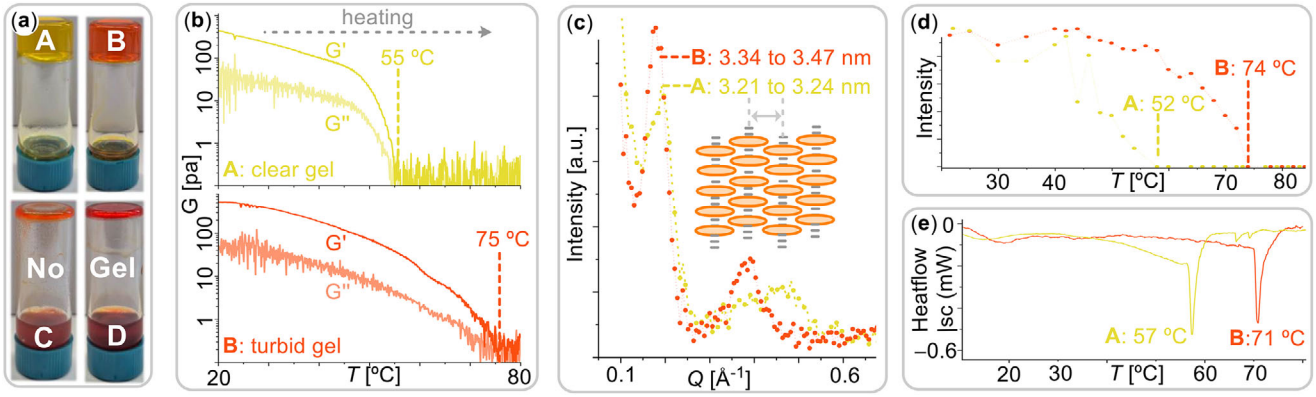

Figure 5. a) Gelation behaviour of **A**-**D** at 3 mg/mL in toluene. b) Temperature dependent rheology heating curve of gels from (top) **A** and (bottom) **B**. c) WAXS spectra of gels. d) Temperature dependence of peak intensities. e) μDSC measurements of gels; second heating curves shown.

process and larger aggregates for **B** than for **A** and this is in line with results from TEM and AFM. Accordingly, rheology reveals the mechanical properties of the gel to be cooling rate dependent, where slower cooling results in stiffer gels (see ESI Figures S36, S37).

To understand how ligand choice favours the assembly of **B** compared to **A**, **C**, and **D**, we employed ab initio calculations using density functional theory (DFT, see ESI Section S10). The geometry optimization of complexes **A**, **B**, **C**, and **D** in the gas phase reveals distinct stable structures (**Figure 6a**). Implicit solvent effects were considered but showed negligible effects on the computational outcomes. Complex **B** adopts a twisted conformation, with its aryloxy oxygens pointing above and below the complex plane. In contrast, complex **A** has a slightly bent shape, complex **D** is more pronouncedly bent, and complex **C** is flat. Among the monomeric complexes, **B** exhibits the highest partial positive charge at the zinc centre (+0.97e, Figure 6b) and the lowest partial negative charge at the oxygen (−0.60e), indicating that it is both the best donor and acceptor in the series and hence should be most prone to stacking via coordinative donor-acceptor interactions. The stand-out acceptor behaviour is qualitatively confirmed in an experiment in which the stoichiometric addition of 4-dimethylaminopyridine (DMAP) as a Lewis base to **A**, **B**, **C**, and **D** respectively resulted in the largest chemical shift ($\Delta\delta$) for the DMAP resonances in the adduct with **B** as a consequence of Lewis base-pair formation (see ESI Figure S45). To evaluate supramolecular polymerization computationally, we constructed stacks of dimers to pentamers by placing optimized monomers approximately 2 Å apart in an eclipsed or helical conformation (see ESI Figure S39) followed by DFT optimization which mimics the self-assembly process (Figure 6c). While all complexes form stable dimers, only **A** and **B** maintain stable trimers, tetramers

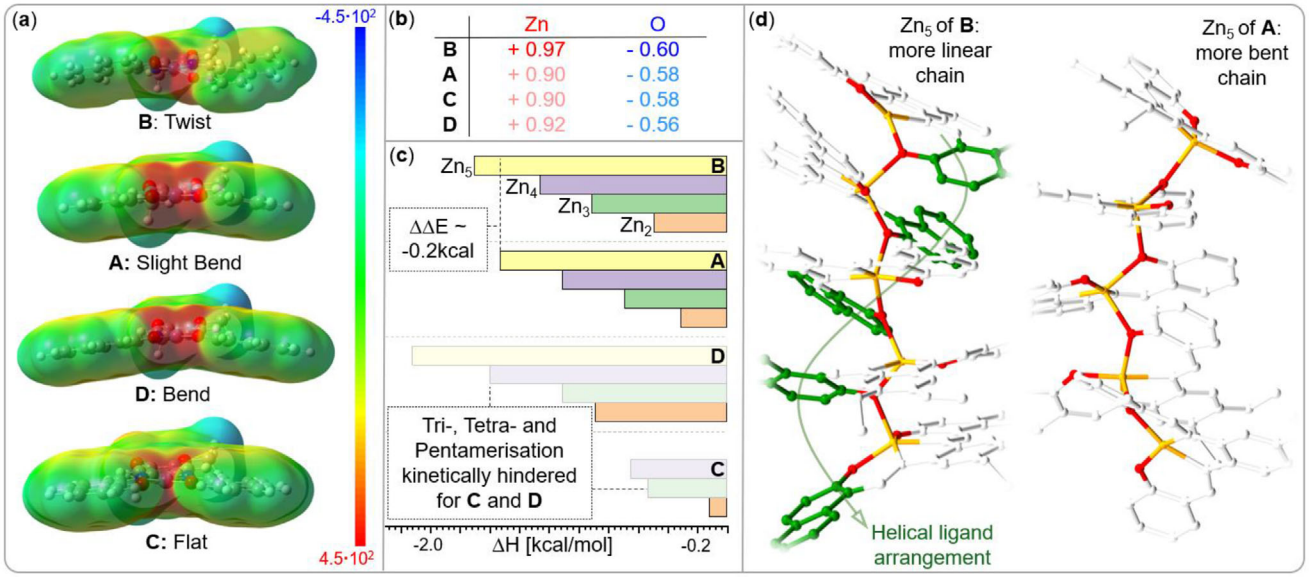

Figure 6. a) Electrostatic potential around the optimised molecular structure of the monomers, alkoxy backbone substituents simplified as methoxy. b) Atomic charge distribution of the Zn(II) and phenolate oxygen centres in the stand-alone complex. c) Dimerisation and oligomerisation enthalpies; faded bars correspond to optimisations that required manual adjustment as outlined in the main text d) Optimised structure of pentamers of **B** and **A**.

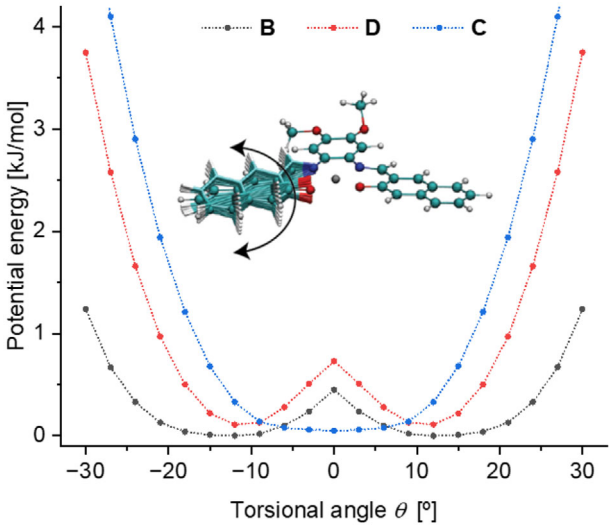

Figure 7. Potential energies for the torsional angle between the plane of one naphthyl moiety and the plane of the remaining complex.

and pentamers. Stacking is more energetically favourable for **B** than for **A**, i.e., ΔE, which is the difference in energy of oligomers versus the analogous number of monomers, being more negative for **B** than for **A** in each oligomerization step. Notably, in these oligomers, the complexes adopt a twisted conformation, which was already the most stable and hence preformed conformation for **B** in the gas phase. While oligomers of **B** optimised into stable structures from both eclipsed and helical starting conformation, oligomers of **A** only did so starting optimisation from the latter. In contrast, **C** and **D** drifted apart during optimization of larger structures than dimers (see supplementary Videos V06–V09), regardless of the initial conformation used, consistent with their experimental behaviour.

However, the thermodynamically favourable dimerization of **C** and **D** suggests that oligomerization should likewise be energetically favoured but is hindered by kinetic barriers. Therefore, we generated the starting structure for the optimization of the trimer, tetramer, and pentamer of **C** and **D**, based on the optimized structure for **B**. For this, we broke the corresponding C—C and C—H bonds of the annulated aryl ring in oligomers of **B** and rotated the fragment while leaving all Zn-O bonds intact to match the respective isomers of **C** and **D** followed by re-optimization. Hereby, the starting geometries already closely match the final ones, so fewer barriers had to be overcome during computational optimization. In doing so, all configurations (except for the pentamer of **D**) that previously drifted apart remained stable during optimization (see supplementary Videos V10–V15). In fact, as shown in (c), now that these barriers are removed, we observe that **C** forms the thermodynamically most stable oligomers which were before prevented to form kinetically.

We hypothesized that the apparent kinetic barrier is related to the flexibility of the complexes and hence performed a conformational scan of **B**, **C**, and **D** assessing the torsional potential during the rotation around one of the C—N single bonds (see **Figure 7**). The energy potential for **C** revealed a minimum at a flat conformation (torsional angle $\theta = 0°$), while **B** and **D** exhibited minima at dihedral angles of 10°–15°, with a local maximum at 0°. These findings are consistent with the optimized structures shown in Figure 6a. Importantly, the potential well represents the energetic barrier for conformational changes in the complexes and is considerably shallower for **B** compared to **C** and **D**. Hence, **B** can undergo structural adaptations more easily, thereby avoiding kinetic traps such as dimers. Combined, our results reveal that **B** is more conformationally flexible than the other complexes to favour polymerisation kinetically while the charge separation in the most stable twisted monomer structure favours polymerisation thermodynamically compared to the other complexes. We infer that these phenomena originate from steric repulsion between the imine —CH═N— and naphthyl hydrogens, opposing the ligand's tendency to flatten because of π-conjugation.

Lastly, DFT also tentatively explains why **B** is more prone to higher order aggregation of the polymer into stiffer fibres than **A**. Comparing the DFT optimised pentamer shows that **B** forms a less bent stack (129° between the outer and middle oxygen atoms of the pentamer, see Figure S44) than **A** (115°) likely due to the steric demand of the more expanded π-system. We infer this results in a more rigid and regular overall geometry of the stack facilitating further aggregation as observed in the TEM and AFM images of the fibres formed from **B** compared to **A**.

Finally, leveraging the coordination chemistry of the metal rather than the ligand likewise enables unique self-assembly behaviour which would not be possible for traditional monomers (**Figure 8**). In this context it is well known that due to the dynamicity of the coordinative bond and the chelate effect, Salphen complexes can be quantitatively obtained from the respective aldehyde and diamine components under metal-templated synthesis.[51] However, this is typically done in coordinating solvents to facilitate solubilisation of the metal salt, which prevents self-assembly. Hence, we hypothesized that conducting the synthesis of **B** in non-coordinating solvents with the appropriate metal precursors allows for direct assembly of fibres from the sub-components of the monomers. Accordingly, we conducted a sub-component self-assembly experiment reacting the diamine component with two equivalents of respective aldehyde and zinc(II) acetyl acetonate, a toluene soluble zinc precursor complex. Indeed, upon cooling the reaction mixture in toluene, gelation occurs as a clear indicator of supramolecular self-assembly. ^{1}H and ^{13}C NMR of the mixture after removal of all volatiles confirms quantitative and selective formation of **B** (see ESI Figures S46, S47). Thus, our system allows for assembly of complex supramolecular architectures directly from the sub-components of the monomers.[60–62] The coordination chemistry of zinc hence allows to combine self-assembly at the molecular level with two hierarchies of self-assembly at the supramolecular level, first into stacks and then into fibres, in the same system.

The coordinative bonds fixing the Zn(II) centres within the monomers maintain dynamicity as the d^{10} electron configuration is not associated with any ligand field stabilisation energy. In contrast, Nickel(II) featuring a d^{8} electron configuration forms more stable complexes within this class of aryloxy-imine ligands. Yet, as discussed above, the red Nickel(II) version **B′** does not undergo self-assembly under the same conditions, as the metal centres are not sufficiently Lewis acidic. Therefore, we added Ni(acac)$_2$ to a toluene gel of **B**. Heating the mixture briefly to 80 °C achieved quantitative transmetallation forming **B′** and Zn(acac)$_2$ as immediately obvious from a colour change from

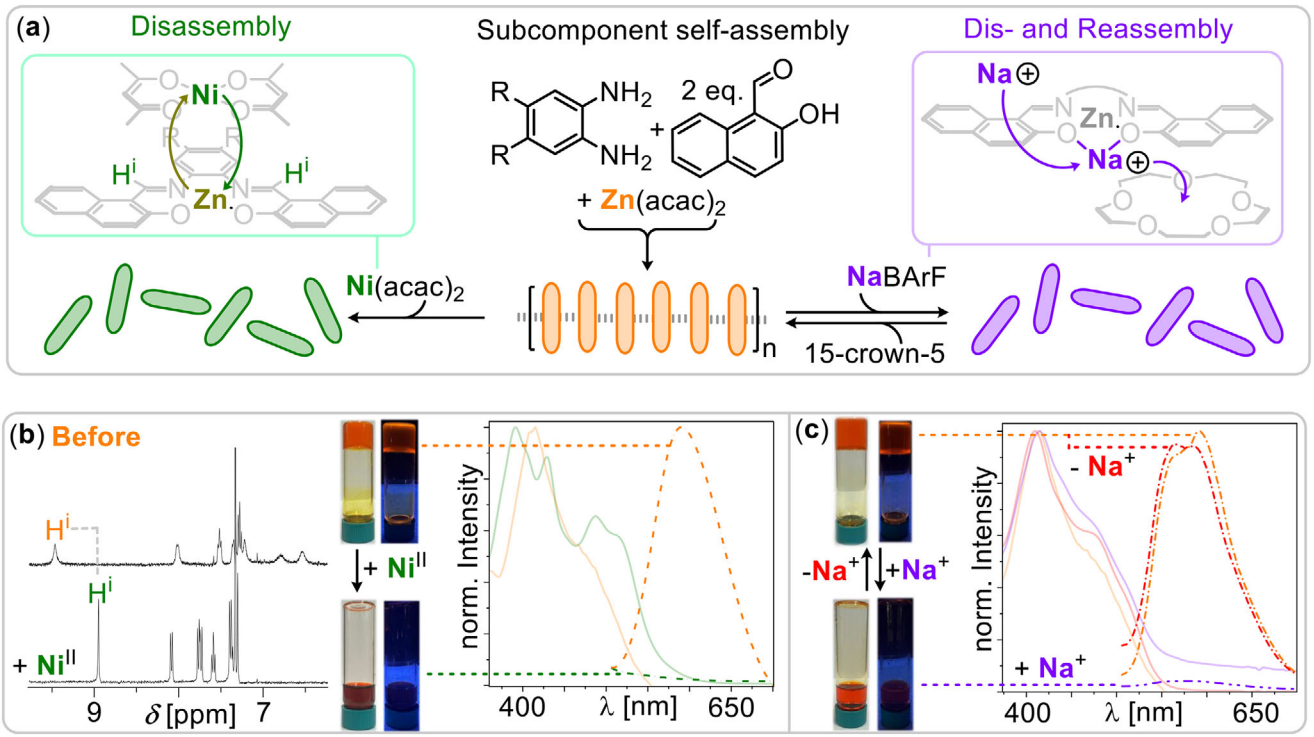

Figure 8. a) Schematic representation of subcomponent self-assembly in toluene as well as coordination induced dis- and reassembly. b) Transmetallation of **B** with $Ni(acac)_2$ leading to liquefying of the gel and luminescence quenching; ^1H NMR spectrum ($CDCl_3$) inset. c) Sodium coordination upon addition of $NaB[(3,5\text{-}(CF_3)_2C_6H_3]_4$ (NaBArF) leading to liquefying of the gel and luminescence quenching which can be reverted via addition of 15-crown-5 scavenging sodium.

orange to red. ^1H NMR confirms transmetallation showing a substantially sharpened as well as shifted spectrum and no luminescence is observed anymore, verifying that no aggregated species are present as shown in Figure 8b. Hence, at room temperature no gel is formed, implying that metal-ligand exchange at the molecular level achieves depolymerisation and disassembly at the supramolecular scale.

However, as nickel(II) coordination within **B'** represents a thermodynamic sink, reverting disassembly could not be achieved. Hence, we hypothesized that in order to achieve reversible control, less stable or inert complexes must be targeted. Close inspection of the mass spectrum of **B** reveals the formation of species $[\mathbf{B}+Na]^+$ at m/z = 981.5310 due to association of **B** with cationic sodium during ionisation of electrospray mass spectrometry (see ESI Figure S10). We infer $[\mathbf{B}+Na]^+$ to be formed via occupation of the second coordination sphere of the ligand in which sodium coordinates to the aryloxy oxygens as shown in Figure 8a.[63] Naturally, due to the lower denticity and coulombic attraction of the coordination site as well as the increased ligand exchange constants of alkali compared to transition metals, sodium coordination must be comparatively unstable and labile which is ideal for reversion of the process. Simultaneously, the positive charge of $[\mathbf{B}+Na]^+$ should lead to repulsion of the complexes disfavouring self-assembly. Accordingly, we added 1 equiv. of $NaB[(3,5\text{-}(CF_3)_2C_6H_3]_4$ (NaBArF), a toluene soluble Na^+ source, to a gelled solution of **B** and observed gradual liquefaction at room temperature. Completing sodium coordination by thermal activation of the mixture consequently prevented gelation upon cooling. Depolymerisation is further substantiated by an approximate 20-fold decrease of the fluorescence (Figure 8c). Comparison of the ^1H NMR spectra before and after sodium coordination reveals substantial broadening of the aromatic resonances of the ligand which we attribute to the formation of different rapidly exchanging interconverting sodium adducts on the NMR timescale spectrometry (see ESI Figure S48). As this indicates labile sodium coordination, we hypothesized that scavenging should be feasible. Accordingly, we added 15-crown-5 displaying an ideal size match for the sodium cation. Luminescence spectroscopy of a dilute solution reveals full recovery of emission intensity upon addition of 15-crown-5. Slow cooling of the reaction mixture (3 mg/mL of **B** in toluene) again results in distinct gelation confirming reconstitution of the self-assembled fibres due to sodium coordination by 15-crown-5.

3. Conclusion

In conclusion, we have established zinc(II) aryloxyimine complexes as a unique system in which gelation and supramolecular self-assembly can be enhanced and controlled by the coordination chemistry of the monomer. Enabled by the flexible coordination sphere of zinc(II), the ligand geometry can be tailored to favour self-assembly both thermodynamically and kinetically. This not only facilitates 1D stacking, but also 3D assembly into higher order morphologies (see electron tomography). Thereby, coordination chemistry cannot only be translated into nanoscopic but also macroscopic

material properties. Having coordination complexes as monomers furthermore allows for assembly of fibres forming emissive gels from the subcomponents of monomers. Disassembly and reassembly by control over the first and second coordination sphere of the ligand grants control over gelation and emission. Ultimately, all phenomena originate from flexible and labile coordinative bonds to metals in the early periods of the periodic table. Hereby, our report demonstrates the largely untapped potential of these in supramolecular self-assembly opening up untapped realms in this field.

Supporting Information

Supporting Information is available from the Wiley Online Library or from the author.

Acknowledgements

We acknowledge funding from the Deutsche Forschungsgemeinschaft (IRTG 2818 OPTEXC, CRC 1449 Dynamic Hydrogels, Core Facility Bio-SupraMol). We thank Dr. Holger Schmalz for assistance with µDSC measurements.

Open access funding enabled and organized by Projekt DEAL.

Conflict of Interest

The authors declare no conflict of interest.

Data Availability Statement

The data that support the findings of this study are available in the supplementary material of this article.

Keywords

DFT calculations, self-assembly, supramolecular polymerisation

Received: March 27, 2025
Revised: May 7, 2025
Published online:

[1] T. Aida, E. w. Meijer, *Isr. J. Chem.* **2020**, *60*, 33.
[2] T. Aida, E. W. Meijer, S. I. Stupp, *Science* **2012**, *335*, 813.
[3] F. García, R. Gómez, L. Sánchez, *Chem. Soc. Rev.* **2023**, *52*, 7524.
[4] M. F. J. Mabesoone, A. R. A. Palmans, E. W. Meijer, *J. Am. Chem. Soc.* **2020**, *142*, 19781.
[5] M. Wehner, F. Würthner, *Nat. Rev. Chem.* **2020**, *4*, 38.
[6] L. Yang, X. Tan, Z. Wang, X. Zhang, *Chem. Rev.* **2015**, *115*, 7196.
[7] S. Datta, S. Takahashi, S. Yagai, *Acc. Mater. Res.* **2022**, *3*, 259.
[8] W. Wagner, M. Wehner, V. Stepanenko, S. Ogi, F. Würthner, *Angew. Chem.* **2017**, *129*, 16224.
[9] S. Sarkar, R. Laishram, D. Deb, S. J. George, *J. Am. Chem. Soc.* **2023**, *145*, 22009.
[10] L. Gallego, J. F. Woods, R. Butti, P. Szwedziak, A. Vargas Jentzsch, M. Rickhaus, *Angew. Chem.* **2024**, *136*, 202318879.
[11] L. Rubert, H. M. A. Ehmann, B. Soberats, *Angew. Chem., Int. Ed.* **2025**, *64*, 20241577.
[12] J. Han, S. Fujikawa, N. Kimizuka, *Angew. Chem.* **2024**, *136*, 202410431.
[13] M. A. Martínez, A. Doncel-Giménez, J. Cerdá, J. Calbo, R. Rodríguez, J. Aragó, J. Crassous, E. Ortí, L. Sánchez, *J. Am. Chem. Soc.* **2021**, *143*, 13281.
[14] L. Kleine-Kleffmann, V. Stepanenko, K. Shoyama, M. Wehner, F. Würthner, *J. Am. Chem. Soc.* **2023**, *145*, 9144.
[15] O. Shyshov, S. V. Haridas, L. Pesce, H. Qi, A. Gardin, D. Bochicchio, U. Kaiser, G. M. Pavan, M. von Delius, *Nat. Commun.* **2021**, *12*, 3134.
[16] M. Endo, T. Fukui, S. H. Jung, S. Yagai, M. Takeuchi, K. Sugiyasu, *J. Am. Chem. Soc.* **2016**, *138*, 14347.
[17] A. Sarkar, R. Sasmal, C. Empereur-mot, D. Bochicchio, S. V. K. Kompella, K. Sharma, S. Dhiman, B. Sundaram, S. S. Agasti, G. M. Pavan, S. J. George, *J. Am. Chem. Soc.* **2020**, *142*, 7606.
[18] H. Kong, A. Valverde-González, R. Maruchenko, L. Bouteiller, M. Raynal, *Angew. Chem.* **2024**, *64*, 202421991.
[19] J. J. B. van der Tol, G. Vantomme, E. W. Meijer, *J. Am. Chem. Soc.* **2023**, *145*, 17987.
[20] L. Đorđević, H. Sai, Y. Yang, N. A. Sather, L. C. Palmer, S. I. Stupp, *Angew. Chem., Int. Ed.* **2023**, *62*, 202214997.
[21] A. Dannenhoffer, H. Sai, E. P. Bruckner, L. Đorđević, A. Narayanan, Y. Yang, X. Ma, L. C. Palmer, S. I. Stupp, *Chem* **2023**, *9*, 170.
[22] V. Saez Talens, J. Davis, C.-H. Wu, Z. Wen, F. Lauria, K. B. S. S. Gupta, R. Rudge, M. Boraghi, A. Hagemeijer, T. T. Trinh, P. Englebienne, I. K. Voets, J. I. Wu, R. E. Kieltyka, *J. Am. Chem. Soc.* **2020**, *142*, 19907.
[23] J. Matern, I. Maisuls, C. A. Strassert, G. Fernández, *Angew. Chem., Int. Ed.* **2022**, *61*, 202208436.
[24] N. Bäumer, J. Matern, G. Fernández, *Chem. Sci.* **2021**, *12*, 12248.
[25] K. Fu, Y. Zhao, G. Liu, *Nat. Commun.* **2024**, *15*, 9571.
[26] A. S.-Y. Law, L. C.-C. Lee, K. K.-W. Lo, V. W.-W. Yam, *J. Am. Chem. Soc.* **2021**, *143*, 5396.
[27] G. Moreno-Alcántar, A. Aliprandi, R. Rouquette, L. Pesce, K. Wurst, C. Perego, P. Brüggeller, G. M. Pavan, L. De Cola, *Angew. Chem.* **2021**, *133*, 5467.
[28] Q. Wan, W.-P. To, X. Chang, C.-M. Che, *Chem* **2020**, *6*, 945.
[29] Y. Ai, M. H.-Y. Chan, A. K.-W. Chan, M. Ng, Y. Li, V. W.-W. Yam, *Proc. Natl. Acad. Sci. USA* **2019**, *116*, 13856.
[30] Q. Wan, W.-P. To, C. Yang, C.-M. Che, *Angew. Chem., Int. Ed.* **2018**, *57*, 3089.
[31] J. Matern, N. Bäumer, G. Fernández, *J. Am. Chem. Soc.* **2021**, *143*, 7164.
[32] N. Bäumer, K. K. Kartha, S. Buss, I. Maisuls, J. P. Palakkal, C. A. Strassert, G. Fernández, *Chem. Sci.* **2021**, *12*, 5236.
[33] H. Zhang, M. H.-Y. Chan, J. Lam, Z. Chen, M.-Y. Leung, E. K.-H. Wong, L. Wu, V. W.-W. Yam, *Chem. Sci.* **2024**, *15*, 8545.
[34] Z. Chen, M. H.-Y. Chan, V. W.-W. Yam, *J. Am. Chem. Soc.* **2020**, *142*, 16471.
[35] N. Bäumer, E. Castellanos, B. Soberats, G. Fernández, *Nat. Commun.* **2023**, *14*, 1084.
[36] J. Matern, K. K. Kartha, L. Sánchez, G. Fernández, *Chem. Sci.* **2020**, *11*, 6780.
[37] A. Aliprandi, M. Mauro, L. De Cola, *Nat. Chem.* **2016**, *8*, 10.
[38] Y. Guo, S. Huang, H. Sun, Z. Wang, Y. Shao, L. Li, Z. Li, F. Song, *J. Mater. Chem. B* **2022**, *10*, 5968.
[39] M. F. J. Mabesoone, A. J. Markvoort, M. Banno, T. Yamaguchi, F. Helmich, Y. Naito, E. Yashima, A. R. A. Palmans, E. W. Meijer, *J. Am. Chem. Soc.* **2018**, *140*, 7810.
[40] S. Ogi, K. Sugiyasu, S. Manna, S. Samitsu, M. Takeuchi, *Nat. Chem.* **2014**, *6*, 188.
[41] N. Sasaki, M. F. J. Mabesoone, J. Kikkawa, T. Fukui, N. Shioya, T. Shimoaka, T. Hasegawa, H. Takagi, R. Haruki, N. Shimizu, S. Adachi, E. W. Meijer, M. Takeuchi, K. Sugiyasu, *Nat. Commun.* **2020**, *11*, 3578.
[42] T. Fukui, S. Kawai, S. Fujinuma, Y. Matsushita, T. Yasuda, T. Sakurai, S. Seki, M. Takeuchi, K. Sugiyasu, *Nat. Chem.* **2017**, *9*, 493.

[43] K. Venkata Rao, D. Miyajima, A. Nihonyanagi, T. Aida, *Nat. Chem.* **2017**, *9*, 1133.
[44] K. Joseph, B. de Waal, S. A. H. Jansen, J. J. B. van der Tol, G. Vantomme, E. W. Meijer, *J. Am. Chem. Soc.* **2024**, *146*, 12130.
[45] I. Robayo-Molina, A. F. Molina-Osorio, L. Guinane, S. A. M. Tofail, M. D. Scanlon, *J. Am. Chem. Soc.* **2021**, *143*, 9060.
[46] S. Sengupta, D. Ebeling, S. Patwardhan, X. Zhang, H. von Berlepsch, C. Böttcher, V. Stepanenko, S. Uemura, C. Hentschel, H. Fuchs, F. C. Grozema, L. D. A. Siebbeles, A. R. Holzwarth, L. Chi, F. Würthner, *Angew. Chem., Int. Ed.* **2012**, *51*, 6378.
[47] F. Helmich, C. C. Lee, M. M. L. Nieuwenhuizen, J. C. Gielen, P. C. M. Christianen, A. Larsen, G. Fytas, P. E. L. G. Leclère, A. P. H. J. Schenning, E. W. Meijer, *Angew. Chem., Int. Ed.* **2010**, *49*, 3939.
[48] C. Liu, K. Liu, A. Mukhopadhyay, V. Paulino, B. Bernard, J.-H. Olivier, *Organometallics* **2020**, *39*, 2984.
[49] N. Sasaki, J. Kikkawa, Y. Ishii, T. Uchihashi, H. Imamura, M. Takeuchi, K. Sugiyasu, *Nat. Chem.* **2023**, *15*, 922.
[50] S. D. Bella, *Dalton Trans.* **2021**, *50*, 6050.
[51] A. W. Kleij, *Dalton Trans.* **2009**, *24*, 4635.
[52] M. V. Escárcega-Bobadilla, G. A. Zelada-Guillén, S. V. Pyrlin, M. Wegrzyn, M. M. D. Ramos, E. Giménez, A. Stewart, G. Maier, A. W. Kleij, *Nat. Commun.* **2013**, *4*, 2648.
[53] J. K.-H. Hui, Z. Yu, M. J. MacLachlan, *Angew. Chem.* **2007**, *119*, 8126.
[54] J. K.-H. Hui, Z. Yu, T. Mirfakhrai, M. J. MacLachlan, *Chem. - Eur. J.* **2009**, *15*, 13456.
[55] J. K.-H. Hui, M. J. MacLachlan, *Dalton Trans.* **2010**, *39*, 7310.
[56] I. P. Oliveri, S. Failla, G. Malandrino, S. Di Bella, *J. Phys. Chem. C* **2013**, *117*, 15335.
[57] X. Song, H. Yu, X. Yan, Y. Zhang, Y. Miao, K. Ye, Y. Wang, *Dalton Trans.* **2018**, *47*, 6146.
[58] G. Salassa, M. J. J. Coenen, S. J. Wezenberg, B. L. M. Hendriksen, S. Speller, J. A. A. W. Elemans, A. W. Kleij, *J. Am. Chem. Soc.* **2012**, *134*, 7186.
[59] D. Silbernagl, M. G. Z. Khorasani, N. C. Murillo, A. M. Elert, H. Sturm, *Beilstein J. Nanotechnol.* **2021**, *12*, 58.
[60] E. G. Percástegui, J. Mosquera, T. K. Ronson, A. J. Plajer, M. Kieffer, J. R. Nitschke, *Chem. Sci.* **2019**, *10*, 2006.
[61] H. Zhu, T. K. Ronson, K. Wu, J. R. Nitschke, *J. Am. Chem. Soc.* **2024**, *146*, 2370.
[62] J. A. Davies, T. K. Ronson, J. R. Nitschke, *J. Am. Chem. Soc.* **2024**, *146*, 5215.
[63] M. W. Drover, *Chem. Soc. Rev.* **2022**, *51*, 1861.